Letter

Infrared study of the multiband low-energy excitations of the topological antiferromagnet $MnBi_2Te_4$

Bing Xu,[1] Y. Zhang,[2] E. H. Alizade,[3] Z. A. Jahangirli,[3,4] F. Lyzwa,[1] E. Sheveleva,[1] P. Marsik,[1] Y. K. Li,[5,6] Y. G. Yao,[5,6] Z. W. Wang,[5,6,*] B. Shen,[2,†] Y. M. Dai,[7] V. Kataev,[8] M. M. Otrokov,[9,10] E. V. Chulkov,[11,12,13] N. T. Mamedov,[3,‡] and C. Bernhard[1,§]

[1]*University of Fribourg, Department of Physics and Fribourg Center for Nanomaterials, Chemin du Musée 3, CH-1700 Fribourg, Switzerland*
[2]*Sate Key Laboratory of Optoelectronic Materials and Technologies, School of Physics, Sun Yat-Sen University, Guangzhou, Guangdong 510275, China*
[3]*Institute of Physics, Azerbaijan National Academy of Sciences, Baku AZ1143, Azerbaijan*
[4]*Baku State University, Z. Khalilov str. 23, AZ1148, Baku, Azerbaijan*
[5]*Key Laboratory of Advanced Optoelectronic Quantum Architecture and Measurement, Ministry of Education, School of Physics, Beijing Institute of Technology, Beijing 100081, China*
[6]*Beijing Key Lab of Nanophotonics and Ultrafine Optoelectronic Systems, Beijing Institute of Technology, Beijing 100081, China*
[7]*National Laboratory of Solid State Microstructures and Department of Physics, Nanjing University, Nanjing 210093, China*
[8]*Leibniz Institute for Solid State and Materials Research IFW Dresden, 01069 Dresden, Germany*
[9]*Centro de Física de Materiales (CFM-MPC), Centro Mixto CSIC-UPV/EHU, 20018 Donostia-San Sebastián, Basque Country, Spain*
[10]*IKERBASQUE, Basque Foundation for Science, 48011 Bilbao, Basque Country, Spain*
[11]*Donostia International Physics Center, 20018 Donostia-San Sebastian, Basque Country, Spain*
[12]*Departamento de Física de Materiales UPV/EHU, 20080 Donostia-San Sebastian, Basque Country, Spain*
[13]*Saint Petersburg State University, Laboratory of Electronic and Spin Structure of Nanosystems, 198504 Saint Petersburg, Russia*

(Received 19 September 2020; accepted 5 February 2021; published 3 March 2021)

With infrared spectroscopy, we studied the bulk electronic properties of the topological antiferromagnet $MnBi_2Te_4$ with $T_N \simeq 25$ K. With the support of band-structure calculations, we assign the intra- and interband excitations and determine the band gap of $E_g \approx 0.17$ eV. We also obtain evidence for two types of conduction bands with light and very heavy carriers. The multiband free-carrier response gives rise to an unusually strong increase of the combined plasma frequency, $\omega_{\rm pl}$, below 300 K. The band reconstruction below T_N yields an additional increase of $\omega_{\rm pl}$ and a splitting of the transition between the two conduction bands by about 54 meV. Our study thus reveals a complex and strongly temperature-dependent multiband low-energy response that has important implications for the study of the surface states and device applications.

DOI: 10.1103/PhysRevB.103.L121103

The research effort on topological quantum materials [1–4] has recently been extended to systems with magnetic order, which enable a variety of field-controlled quantum states [5–13], such as the quantum anomalous Hall (QAH) effect [6–8], the topological axion state [9–12], and Majorana fermions [2,13]. Such materials have been obtained, e.g., by creating heterostructures from magnetic and topological materials or by adding magnetic defects to topological materials. With the latter approach, the QAH effect was realized for the first time in Cr-doped $(Bi, Sb)_2Te_3$ films [7]. The ideal candidates, however, are bulk topological materials with intrinsic magnetic order for which various problems inherent to thin film growth and defect engineering can be avoided.

A promising candidate is $MnBi_2Te_4$ (MBT), which is a topological insulator with A-type antiferromagnetic (AFM) order as predicted by theory [14–17] and recently confirmed by experiments [18–31]. Notably, the bulk AFM transition at $T_N \simeq 25$ K has been predicted to strongly affect the electronic states at the (0001) surface, since it creates a gap on the Dirac cone [14–16,18]. Moreover, for thin films the topological properties should depend on the number of MBT layers such that an axion insulator or a QAH insulator appears for even and odd numbers, respectively [14,15]. A quantized Hall conductance has indeed been observed in few-layer MBT films [26–28], albeit only in magnetic fields of 5–10 T that change the magnetic order to a ferromagnetic one [27,28]. The properties of the surface of MBT single crystals are also debated. For example, the formation of a gap below T_N of the Dirac cone at the (0001) surface is seen in some angle-resolved photoemission spectroscopy (ARPES) studies [18–21] but not in others [32–36]. This calls for further studies of the surface structural and magnetic properties [33]. Likewise, the bulklike low-energy excitations and their modification in the AFM state are still not fully understood.

Here we study the bulk electronic properties of $MnBi_2Te_4$ crystals with infrared spectroscopy. In combination with band-structure calculations, we assign the intra- and interband excitations and estimate the inverted bulk band gap and the

*zhiweiwang@bit.edu.cn
†shenbing@mail.sysu.edu.cn
‡n.mamedov@physics.ab.az
§christian.bernhard@unifr.ch

 ©2021 American Physical Society

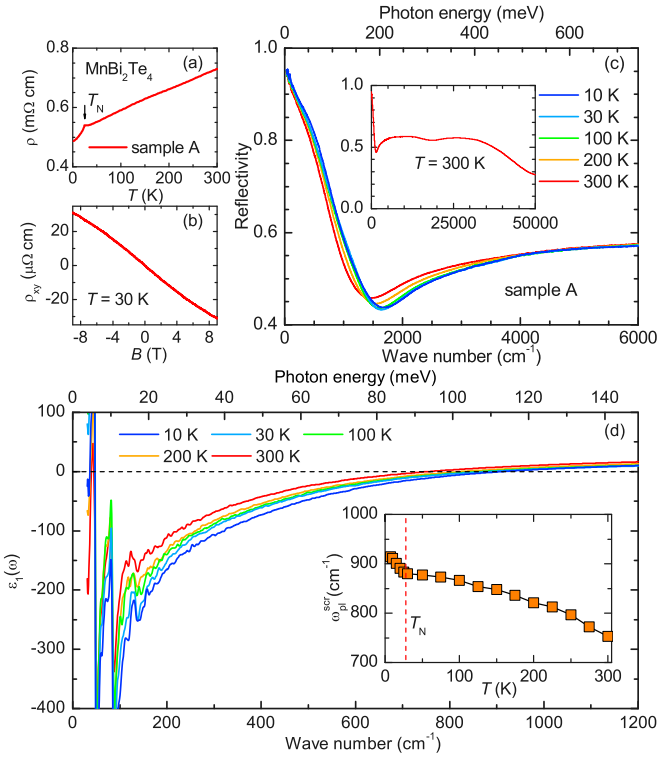

FIG. 1. (a) T-dependent resistivity of the $MnBi_2Te_4$ sample A. The arrow marks the AFM transition at $T_N \simeq 25$ K. (b) Hall resistance R_{xy} of sample A at 30 K. (c) T dependence of the reflectivity up to 6000 cm^{-1}. Inset: Spectrum up to 50 000 cm^{-1} at 300 K. (d) T dependence of the real part of the dielectric function $\varepsilon_1(\omega)$. Inset: Screened plasma frequency obtained from the zero crossing of $\varepsilon_1(\omega)$.

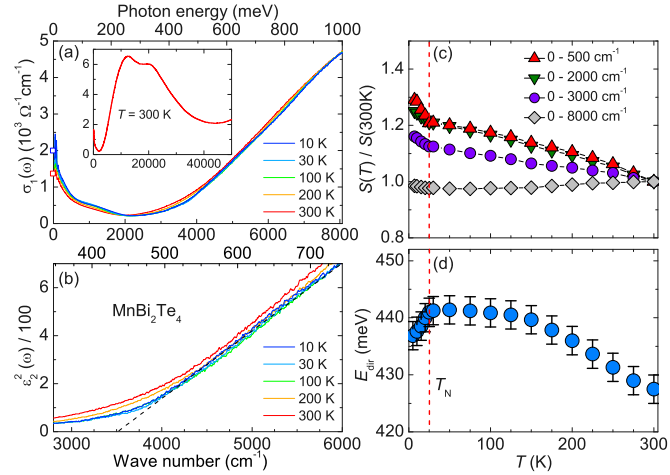

FIG. 2. (a) T-dependent optical conductivity of $MnBi_2Te_4$ up to 8000 cm^{-1}. The symbols on the y axis denote σ_{DC} at 10 and 300 K from the transport data in Fig. 1(a). Inset: Spectrum up to 50 000 cm^{-1} at 300 K. (b) T-dependent spectra of $\epsilon_2^2(\omega)$. The dashed line shows a linear extrapolation toward the zero crossing of $\epsilon_2^2(\omega)$ to obtain the onset of the direct interband transitions, E_{dir}. (c) T dependence of the spectral weight for different cutoff frequencies. (d) T dependence of E_{dir}.

chemical potential. We also study the excitations of the free carriers and determine their plasma frequency. The latter has a surprisingly low value and an unusual T dependence, with a pronounced anomaly below T_N. We show that this anomalous behavior can be explained in terms of two conduction bands with largely different effective masses. Below T_N we also identify a splitting of the transitions between the light and heavy conduction bands (by about 54 meV) that arises from the magnetic coupling between the conduction electrons and the localized Mn moments and agrees with the one seen with ARPES [34–37]. This information about the multiband nature of the free carriers and their low-energy excitations is a prerequisite for understanding the plasmonic properties in the bulk as well as of the surface states and their eventual device applications. In the first place, it calls for attempts to reduce the defect concentration and thus the n-type doping such that a simpler single band picture applies.

Two batches of MBT single crystals were grown with a flux method [31] at Sun Yat-Sen University (Sample A) and Beijing Institute of Technology (Sample B). Both have a metallic in-plane resistivity with an anomaly around $T_N \simeq 25$ K, as shown in Fig. 1(a) for sample A. The negative Hall-resistivity ρ_{xy} of sample A in Fig. 1(b) indicates electronlike carriers with a concentration of $n = 1.7 \times 10^{20}\,cm^{-3}$, in agreement with most previous studies [21–23,38,39]. Details about the infrared reflectivity measurements and the Kramers-Kronig analysis are given in Sec. A of the supplemental material (SM) [40].

Figure 1(c) shows for sample A the temperature (T) - dependent reflectivity $R(\omega)$ up to 6000 cm^{-1}. The inset shows the room-temperature spectrum up to 50 000 cm^{-1}. Below about 1500 cm^{-1} there is a sharp upturn of $R(\omega)$ toward unity that is characteristic of a plasma edge due to the itinerant carriers. This plasma edge shifts to higher frequency as the T decreases, indicating an enhancement of free carrier density, n, or a reduction of effective mass, m^*. Very similar spectra have been obtained for sample B (see Sec. B in the SM [40]), thus the following discussion is focused on sample A.

Figure 1(d) displays the T dependence of the real part of the dielectric function $\varepsilon_1(\omega)$. The spectra reveal an inductive behavior with a downturn of $\varepsilon_1(\omega)$ toward negative values at low frequency that is another hallmark of a metallic response. The sharp features at 47, 84, and 133 cm^{-1} are infrared-active phonons that are not discussed further here. The horizontal dashed line shows the zero crossing of $\varepsilon_1(\omega)$, which marks the screened plasma frequency $\omega_{pl}^{scr} = \omega_{pl}/\sqrt{\varepsilon_\infty}$, where ε_∞ is the high-frequency dielectric constant and $\omega_{pl} = \sqrt{ne^2/\epsilon_0 m^*}$ is the free-carrier plasma frequency. The inset details the T dependence of ω_{pl}^{scr}, which reveals an unusually large increase from about 750 cm^{-1} at 300 K to 880 cm^{-1} at 30 K. There is also a sudden, additional increase below T_N to about 910 cm^{-1} at 10 K, which provides a first spectroscopic indication that the AFM order has a pronounced effect on the electronic properties.

Figure 2(a) displays the T dependence of the real part of the optical conductivity $\sigma_1(\omega)$ up to 8000 cm^{-1}. The inset shows the 300 K spectrum up to 50 000 cm^{-1} which is dominated by two interband transitions with bands around 12 500 and 20 000 cm^{-1}, in agreement with Ref. [45]. The optical response below 8000 cm^{-1} consists of a Drude peak with a tail extending to about 2000 cm^{-1} that is well separated from the onset of strong interband transitions above 3000 cm^{-1}.

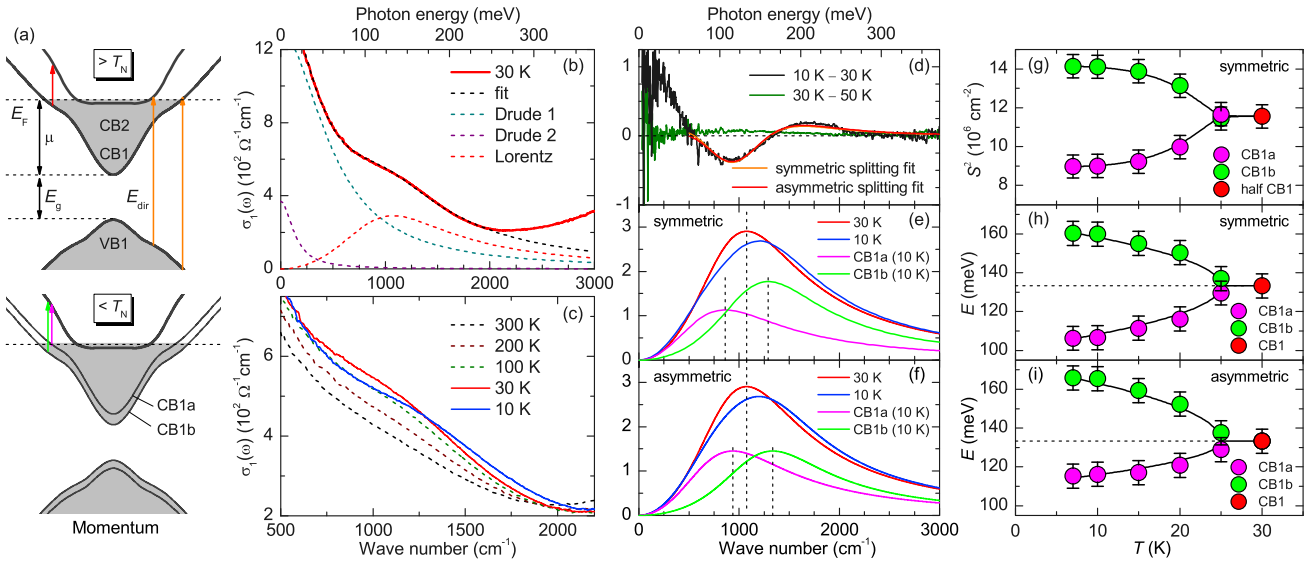

FIG. 3. (a) Schematic of the band structure of $MnBi_2Te_4$ in the paramagnetic (upper panel) and AFM (lower panel) states. (b) Drude-Lorentz fit of the conductivity at 30 K around the lowest interband-transition. (c) T-dependent spectra showing the anomaly below $T_N \simeq 25$ K. (d) Difference plots of $\sigma_1(\omega)$ and corresponding fits of the band splitting. Lorentz fits of the low-energy interband transition at 30 and 10 K and of the split bands at 10 K assuming (e) a symmetric and (f) an asymmetric band splitting. T dependence of the fit parameters of the split bands obtained (g) and (h) with the symmetric and (i) the asymmetric model.

The Drude peak grows upon cooling, consistent with the increase of $\omega_{\rm pl}^{\rm scr}$ in Fig. 1(d). The dc conductivity data at 10 and 300 K from Fig. 1(a) (squares on the y-axis) agree with the zero-frequency extrapolation of $\sigma_1(\omega)$. The width of the Drude peak of about 500 cm^{-1} is nearly T-independent and much larger than, e.g., in Bi_2Te_3 [46]. The scattering thus seems to be dominated by disorder effects, e.g., due to Mn-Bi antisite defects [19]. The T dependence of the onset of the strong interband transitions, $E_{\rm dir}$, that are most likely direct transitions across the band gap, E_g, between the valence band (VB) and the conduction band (CB), has been obtained with a linear extrapolation of $\epsilon_2^2(\omega)$, as shown in Fig. 2(b). It increases toward low T, but it decreases suddenly below T_N [see Fig. 2(d)].

The spectral changes have been further analyzed by calculating the evolution of the spectral weight (SW), $S(\omega_c) = \int_0^{\omega_c} \sigma_1(\omega) d\omega$, for different cutoff frequencies ω_c. Figure 2(c) shows the T dependence of the ratio $S(\omega_c, T)/S(\omega_c, T = 300\ {\rm K})$ at representative cutoffs. At $\omega_c = 500$ and 2000 cm^{-1}, where the free-carrier response dominates, the SW increases toward low T and exhibits an additional upturn below T_N, in agreement with the trend of $\omega_{\rm pl}^{\rm scr}$ in Fig. 1(d). At the higher cutoffs, this increase becomes less pronounced until at $\omega_c = 8000$ cm^{-1} (1 eV) it is almost constant. This confirms that the SW redistribution is confined to energies below 1 eV.

Next, we analyze in more detail the response below 2000 cm^{-1}, which contains in addition to the Drude response a weak band due to a low-energy interband transition. This is evident in Fig. 3(b), which displays the $\sigma_1(\omega)$ spectrum at 30 K together with a Drude-Lorentz fit. It reveals a band centered around 1100 cm^{-1} that overlaps with the tail of the Drude response. The fit function contains two Drude-terms with different plasma frequencies and scattering rates of $\omega_{\rm pl,1} = 6215$ cm^{-1}, $1/\tau_1 = 520$ cm^{-1} and $\omega_{\rm pl,2} = 1870$ cm^{-1}, $1/\tau_2 = 150$ cm^{-1}, respectively. The band at 1100 cm^{-1} is described by a Lorentz function. Details about the Drude-Lorentz analysis are given in Sec. C of the SM [40].

Figure 3(a) shows a schematic of the band structure in the vicinity of the chemical potential that is consistent with our optical data, with our band calculations along the Γ-Y direction (see Sec. E in the SM [40]) and also with reported ARPES data [33–35]. In addition to a pair of conduction and valence bands that is forming an inverted band gap (CB1 and VB1), it contains a second conduction band (CB2) that is located slightly above CB1 and has a very flat bottom and thus a very large effective mass. As shown in the following, our optical data suggest that the chemical potential, μ, is crossing both CB1 and CB2 (at low temperature). This assignment is consistent with the use of two Drude-peaks in fitting the low-energy response in the previous paragraph. It also accounts for the weak band around 1100 cm^{-1} in terms of the interband transitions between CB1 and CB2 (red arrow). The optical excitations at higher energy involve transitions across the direct band gap E_g, from the VB to the empty states in CB1 and CB2, as illustrated in Fig. 3(a) by the orange arrows. Note that if μ would not be crossing CB2, the transition between the top of VB1 and the bottom of CB2, which are both rather flat and optically allowed, would give rise to a strong peak near $E_{\rm dir}$ that is clearly not seen in the spectra of Fig. 2(a). On the other hand, a pronounced peak around 3350 cm^{-1} (415 meV) has been observed in the corresponding spectra, which were taken on the as-grown surface of the same sample (see Sec. D in the SM [40]). This implies that for the as-grown surface, the chemical potential is somewhat lower, such that it falls below CB2. Such a reduction of the free-carrier concentration might be caused, for example, by the localization of carries on extrinsic defects or by a lower

concentration of intrinsic defects that are responsible for the n-type doping.

With this band assignment, we can estimate for the cleaved MBT surfaces the low-T value of the chemical potential μ by using the expressions $\mu = \hbar^2 k_F^2/2m^* = (\hbar^2/2m^*)(6\pi^2 n/g_s g_b)^{2/3}$, with the Fermi vector k_F, the carrier density $n = \frac{1}{(2\pi)^3}\frac{4}{3}\pi k_F^3 g_s g_b$, and the spin and band degeneracies $g_s = 2$ and $g_b = 2$ [15,16,47]. Using $n_1 = 0.517 \times 10^{20}$ cm^{-3} and $n_2 = 1.183 \times 10^{20}$ cm^{-3} (see Sec. C in the SM [40]), as well as $m_1^* = 0.12 m_e$ and $m_2^* = 3 m_e$ according to the band-structure calculations (see Sec. E in the SM [40]), we derive $\mu_1 = 0.266$ eV and $\mu_2 = 0.019$ eV for CB1 and CB2, respectively. Accordingly, with an estimate of $E_{\rm dir} \simeq 0.415$ eV for the direct interband transition between VB1 and CB2 around the Γ point, we derive a band gap of $E_g \approx E_{\rm dir} + \mu_2 - \mu_1 = 0.17 \pm 0.02$ eV at 30 K (as explained in Sec. F of the SM [40], the largest uncertainty arises from the estimate of μ_2), which agrees well with the reported values from band calculations and ARPES [15–21,33–35].

Next, we focus on the band reconstruction below T_N, especially on the anomalous changes of the interband transition at 1100 cm^{-1}, which provide evidence for a magnetic splitting of CB1. In the paramagnetic state, the $\sigma_1(\omega)$ spectra in Fig. 3(c) exhibit a monotonic increase in this frequency range that arises mainly from the growth of the Drude SW, as shown in Figs. 1(d) and 2(c). Below T_N, this trend is suddenly interrupted, i.e., $\sigma_1(\omega)$ decreases from about 500–1200 cm^{-1} whereas it gets anomalously enhanced between 1200 and 2000 cm^{-1}. These anomalous changes, which are detailed in Fig. 3(d) in terms of the difference spectrum of $\sigma_1(\omega)$ at 30 and 10 K, are characteristic of a splitting of the conduction band CB1 into CB1a and CB1b, as indicated in the lower panel of Fig. 3(a). An additional contribution that arises from a much weaker and almost featureless T-dependent change of the background, which occurs also above T_N, has been corrected using the difference between 30 and 50 K (olive line). This band splitting, which is caused by the exchange interaction of the conduction electrons with the Mn moments, which lifts the band degeneracy due to the unit cell doubling in the AFM state, is also seen in recent ARPES studies [34–37]. Note that the magnetic splitting of CB2 is assumed to be much smaller and thus is neglected. This assumption is supported by ARPES data [34–37], and also by a comparison of the density of states at the Fermi level derived from our optical data with the Korringa-slope of the ESR data in Ref. [18], as outlined in Sec. H of the SM [40]. The successful modeling of the data in Fig. 3(d) confirms that the spectral changes below T_N arise from a corresponding splitting of the interband transitions from CB1a to CB2 and CB1b to CB2. It has been obtained with the function $\Delta\sigma_1(\omega) = L_a(\omega_a, \gamma_a, S_a) + L_b(\omega_b, \gamma_b, S_b) - L(\omega_0, \gamma, S)$, for which L represents the Lorentz function, and the subscripts a and b denote the interband transitions from the split bands. The parameters in the paramagnetic state have been obtained from a Drude-Lorentz fit at 30 K. We have used two different approaches to model the changes below T_N. The first one assumes a symmetric splitting of the bands with $|\omega_a - \omega_0| = |\omega_b - \omega_0|$, $\gamma_a = \gamma_b = \gamma$, and $S_a^2 + S_b^2 = S^2$. The second one allows for an asymmetric band splitting but fixes their spectral weights to $|\omega_a - \omega_0| \neq |\omega_b - \omega_0|$, $\gamma_a = \gamma_b = \gamma$, and $S_a^2 = S_b^2 = S^2/2$. The orange and red curves in Fig. 3(d) show that both models allow us to reproduce the S-shaped feature of $\sigma_1(\omega, 10\,{\rm K}) - \sigma_1(\omega, 30\,{\rm K})$. The contributions of the individual bands CB1a and CB1b as obtained from the two models are shown in Figs. 3(e) and 3(f), respectively. The symmetric model yields a splitting of $|\omega_a - \omega_0| = |\omega_b - \omega_0| = 27$ meV at 10 K, and for the asymmetric one it amounts to $|\omega_b - \omega_0| = 32$ meV and $|\omega_a - \omega_0| = 17$ meV. The T dependence of the obtained fit parameters is displayed in Fig. 3(g) for the weights S_a^2 and S_b^2 obtained with symmetric band splitting and in Figs. 3(h) and 3(i) for the corresponding positions ω_a and ω_b for the symmetric and asymmetric models, respectively. Note that the splitting of CB1 (and likely a corresponding splitting of VB1) can also account for the anomalous decrease of $E_{\rm dir}$ below T_N, since it reduces E_g.

Finally, we return to the unusually large increase of $\omega_{\rm pl}^2$ toward low T and its pronounced anomaly below T_N. The ∼20% increase between 300 and 30 K can hardly arise from a volume contraction effect that would imply a giant expansion coefficient of 4×10^{-3} K^{-1}. Likewise, the anomalous increase of $\omega_{\rm pl}^2$ below T_N would require unrealistically large magnetostriction effects. Instead, we propose that the strong increase of $\omega_{\rm pl}^2$ toward low T results from an exchange of conduction electrons between the light and very heavy states in CB1 and CB2 [48–52]. Due to their largely different effective masses, the distribution of electrons is strongly dependent on the relative position of CB1 and CB2 with respect to the chemical potential. Accordingly, the T dependence of the chemical potential accounts for the observed change of $\omega_{\rm pl}^2$ in the paramagnetic state (see Sec. F in the SM [40]). The anomalous increase of $\omega_{\rm pl}^2$ below T_N requires in addition a small shift of the center of CB1a and CB1b against CB2 of ∼10 meV (see Sec. G in the SM [40]), which is indeed comparable to the shift obtained with the asymmetric band-splitting model in Figs. 3(f) and 3(i). Note that the corresponding effect of the magnetic slitting of CB1a and CB1b is weaker and of the opposite sign (see Sec. G in the SM [40]).

We would also like to mention that for the majority of degenerate doped narrow gap semiconductors, $\omega_{\rm pl}$ exhibits a much weaker T dependence and usually decreases upon cooling due to the freeze-out of carriers. Interestingly, another rare exception, for which $\omega_{\rm pl}^2$ exhibits a similarly strong increase toward low T, is Bi_2Te_3. While the samples studied in Ref. [53] were hole-doped, in analogy to MBT, they may also have light and very heavy valence electrons.

In summary, we determined the bulk, optical properties of the AFM topological insulator $MnBi_2Te_4$. In combination with band-structure calculations, we assigned the intra- and interband excitations and obtained a bulk band gap of $E_g \approx 0.17$ eV. We also provided evidence for two conduction bands with largely different effective masses of 0.12 and 3 m_e and chemical potentials of 0.266 and 0.019 eV (at 30 K). A T-dependent transfer of electrons between these conduction bands and the subsequent change of the average effective mass can account for an unusually strong T dependence of the free-carrier plasma frequency, $\omega_{\rm pl}$. Below $T_N \simeq 25$ K, we observed clear signs of a band reconstruction in terms of an additional, anomalous increase of $\omega_{\rm pl}$ and a splitting of

the transition between the conduction bands. This detailed information about the bulk band structure and the multiband charge-carrier response is a prerequisite for the understanding of the plasmonic properties of the bulk and surface states and their device applications.

We acknowledge discussions with A. Akrap, G. Khalliulin, and Z. Rukelj. The work in Fribourg was supported by the Schweizerische Nationalfonds (SNF) through Grant No. 200020-172611. V.K. acknowledges support by the Deutsche Forschungsgemeinschaft (DFG) through Grant No. KA1694/12-1. N.M. acknowledges the support of the Science Development Foundation under the President of the Republic of Azerbaijan (Grant No. EİF-BGM-4-RFTF-1/2017-21/04/1-M-02). The work at Beijing was supported by the Natural Science Foundation of China (NSFC Grant No. 11734003), the National Key R&D Program of China (Grants No. 2016YFA0300600 and No. 2020YFA0308800), and the Beijing Natural Science Foundation (Grant No. Z190006). Z.W. acknowledges the support from Beijing Institute of Technology Research Fund Program for Young Scholars. B.S. acknowledges the support of the Fundamental Research Funds for the Central Universities, Grant No. 19lgpy260. E.V.C. acknowledges Saint Petersburg State University (Grant No. ID 73028629). Y.M.D. acknowledges the support of the Natural Science Foundation of China (Grant No. 11874206). M.M.O. acknowledges the support by Spanish Ministerio de Ciencia e Innovación (Grant No. PID2019-103910GB-I00).

[1] M. Z. Hasan and C. L. Kane, Rev. Mod. Phys. **82**, 3045 (2010).
[2] X.-L. Qi and S.-C. Zhang, Rev. Mod. Phys. **83**, 1057 (2011).
[3] F. D. M. Haldane, Rev. Mod. Phys. **89**, 040502 (2017).
[4] Y. Tokura, K. Yasuda, and A. Tsukazaki, Nat. Rev. Phys. **1**, 126 (2019).
[5] X. Wan, A. M. Turner, A. Vishwanath, and S. Y. Savrasov, Phys. Rev. B **83**, 205101 (2011).
[6] R. Yu, W. Zhang, H.-J. Zhang, S.-C. Zhang, X. Dai, and Z. Fang, Science **329**, 61 (2010).
[7] C.-Z. Chang, J. Zhang, X. Feng, J. Shen, Z. Zhang, M. Guo, K. Li, Y. Ou, P. Wei, L.-L. Wang, Z.-Q. Ji, Y. Feng, S. Ji, X. Chen, J. Jia, X. Dai, Z. Fang, S.-C. Zhang, K. He, Y. Wang, L. Lu, X.-C. Ma, and Q.-K. Xue, Science **340**, 167 (2013).
[8] C.-Z. Chang, W. Zhao, D. Y. Kim, H. Zhang, B. A. Assaf, D. Heiman, S.-C. Zhang, C. Liu, M. H. W. Chan, and J. S. Moodera, Nat. Mater. **14**, 473 (2015).
[9] X.-L. Qi, T. L. Hughes, and S.-C. Zhang, Phys. Rev. B **78**, 195424 (2008).
[10] A. M. Essin, J. E. Moore, and D. Vanderbilt, Phys. Rev. Lett. **102**, 146805 (2009).
[11] R. S. K. Mong, A. M. Essin, and J. E. Moore, Phys. Rev. B **81**, 245209 (2010).
[12] D. Xiao, J. Jiang, J.-H. Shin, W. Wang, F. Wang, Y.-F. Zhao, C. Liu, W. Wu, M. H. W. Chan, N. Samarth, and C.-Z. Chang, Phys. Rev. Lett. **120**, 056801 (2018).
[13] Q. L. He, L. Pan, A. L. Stern, E. C. Burks, X. Che, G. Yin, J. Wang, B. Lian, Q. Zhou, E. S. Choi, K. Murata, X. Kou, Z. Chen, T. Nie, Q. Shao, Y. Fan, S.-C. Zhang, K. Liu, J. Xia, and K. L. Wang, Science **357**, 294 (2017).
[14] M. M. Otrokov, I. P. Rusinov, M. Blanco-Rey, M. Hoffmann, A. Y. Vyazovskaya, S. V. Eremeev, A. Ernst, P. M. Echenique, A. Arnau, and E. V. Chulkov, Phys. Rev. Lett. **122**, 107202 (2019).
[15] J. Li, Y. Li, S. Du, Z. Wang, B.-L. Gu, S.-C. Zhang, K. He, W. Duan, and Y. Xu, Sci. Adv. **5**, eaaw5685 (2019).
[16] D. Zhang, M. Shi, T. Zhu, D. Xing, H. Zhang, and J. Wang, Phys. Rev. Lett. **122**, 206401 (2019).
[17] J. Li, C. Wang, Z. Zhang, B.-L. Gu, W. Duan, and Y. Xu, Phys. Rev. B **100**, 121103(R) (2019).
[18] M. M. Otrokov, I. I. Klimovskikh, H. Bentmann, D. Estyunin, A. Zeugner, Z. S. Aliev, S. Gaß, A. U. B. Wolter, A. V. Koroleva, A. M. Shikin, M. Blanco-Rey, M. Hoffmann, I. P. Rusinov, A. Y. Vyazovskaya, S. V. Eremeev, Y. M. Koroteev, V. M. Kuznetsov, F. Freyse, J. Sánchez-Barriga, I. R. Amiraslanov, M. B. Babanly, N. T. Mamedov, N. A. Abdullayev, V. N. Zverev, A. Alfonsov, V. Kataev, B. Büchner, E. F. Schwier, S. Kumar, A. Kimura, L. Petaccia, G. Di Santo, R. C. Vidal, S. Schatz, K. Kißner, M. Ünzelmann, C. H. Min, S. Moser, T. R. F. Peixoto, F. Reinert, A. Ernst, P. M. Echenique, A. Isaeva, and E. V. Chulkov, Nature (London) **576**, 416 (2019).
[19] A. Zeugner, F. Nietschke, A. U. B. Wolter, S. Gaß, R. C. Vidal, T. R. F. Peixoto, D. Pohl, C. Damm, A. Lubk, R. Hentrich, S. K. Moser, C. Fornari, C. H. Min, S. Schatz, K. Kißner, M. Ünzelmann, M. Kaiser, F. Scaravaggi, B. Rellinghaus, K. Nielsch, C. Hess, B. Büchner, F. Reinert, H. Bentmann, O. Oeckler, T. Doert, M. Ruck, and A. Isaeva, Chem. Mater. **31**, 2795 (2019).
[20] R. C. Vidal, H. Bentmann, T. R. F. Peixoto, A. Zeugner, S. Moser, C.-H. Min, S. Schatz, K. Kißner, M. Ünzelmann, C. I. Fornari, H. B. Vasili, M. Valvidares, K. Sakamoto, D. Mondal, J. Fujii, I. Vobornik, S. Jung, C. Cacho, T. K. Kim, R. J. Koch, C. Jozwiak, A. Bostwick, J. D. Denlinger, E. Rotenberg, J. Buck, M. Hoesch, F. Diekmann, S. Rohlf, M. Kalläne, K. Rossnagel, M. M. Otrokov, E. V. Chulkov, M. Ruck, A. Isaeva, and F. Reinert, Phys. Rev. B **100**, 121104(R) (2019).
[21] S. H. Lee, Y. Zhu, Y. Wang, L. Miao, T. Pillsbury, H. Yi, S. Kempinger, J. Hu, C. A. Heikes, P. Quarterman, W. Ratcliff, J. A. Borchers, H. Zhang, X. Ke, D. Graf, N. Alem, C.-Z. Chang, N. Samarth, and Z. Mao, Phys. Rev. Research **1**, 012011(R) (2019).
[22] J.-Q. Yan, Q. Zhang, T. Heitmann, Z. Huang, K. Y. Chen, J.-G. Cheng, W. Wu, D. Vaknin, B. C. Sales, and R. J. McQueeney, Phys. Rev. Mater. **3**, 064202 (2019).
[23] J. Cui, M. Shi, H. Wang, F. Yu, T. Wu, X. Luo, J. Ying, and X. Chen, Phys. Rev. B **99**, 155125 (2019).
[24] Y. Gong, J. Guo, J. Li, K. Zhu, M. Liao, X. Liu, Q. Zhang, L. Gu, L. Tang, X. Feng, D. Zhang, W. Li, C. Song, L. Wang, P. Yu, X. Chen, Y. Wang, H. Yao, W. Duan, Y. Xu, S.-C. Zhang, X. Ma, Q.-K. Xue, and K. He, Chinese Phys. Lett. **36**, 076801 (2019).
[25] J.-Q. Yan, S. Okamoto, M. A. McGuire, A. F. May, R. J. McQueeney, and B. C. Sales, Phys. Rev. B **100**, 104409 (2019).
[26] Y. Deng, Y. Yu, M. Z. Shi, Z. Guo, Z. Xu, J. Wang, X. H. Chen, and Y. Zhang, Science **367**, 895 (2020).

[27] C. Liu, Y. Wang, H. Li, Y. Wu, Y. Li, J. Li, K. He, Y. Xu, J. Zhang, and Y. Wang, Nat. Mater. **19**, 522 (2020).
[28] J. Ge, Y. Liu, J. Li, H. Li, T. Luo, Y. Wu, Y. Xu, and J. Wang, Natl. Sci. Rev. **7**, 1280 (2020).
[29] C. Hu, K. N. Gordon, P. Liu, J. Liu, X. Zhou, P. Hao, D. Narayan, E. Emmanouilidou, H. Sun, Y. Liu, H. Brawer, A. P. Ramirez, L. Ding, H. Cao, Q. Liu, D. Dessau, and N. Ni, Nat. Commun. **11**, 97 (2020).
[30] J. Wu, F. Liu, M. Sasase, K. Ienaga, Y. Obata, R. Yukawa, K. Horiba, H. Kumigashira, S. Okuma, T. Inoshita, and H. Hosono, Sci. Adv. **5**, eaax9989 (2019).
[31] B. Chen, F. Fei, D. Zhang, B. Zhang, W. Liu, S. Zhang, P. Wang, B. Wei, Y. Zhang, Z. Zuo, J. Guo, Q. Liu, Z. Wang, X. Wu, J. Zong, X. Xie, W. Chen, Z. Sun, S. Wang, Y. Zhang, M. Zhang, X. Wang, F. Song, H. Zhang, D. Shen, and B. Wang, Nat. Commun. **10**, 4469 (2019).
[32] D. Nevola, H. X. Li, J. Q. Yan, R. G. Moore, H. N. Lee, H. Miao, and P. D. Johnson, Phys. Rev. Lett. **125**, 117205 (2020).
[33] Y.-J. Hao, P. Liu, Y. Feng, X.-M. Ma, E. F. Schwier, M. Arita, S. Kumar, C. Hu, R. Lu, M. Zeng, Y. Wang, Z. Hao, H.-Y. Sun, K. Zhang, J. Mei, N. Ni, L. Wu, K. Shimada, C. Chen, Q. Liu, and C. Liu, Phys. Rev. X **9**, 041038 (2019).
[34] Y. J. Chen, L. X. Xu, J. H. Li, Y. W. Li, H. Y. Wang, C. F. Zhang, H. Li, Y. Wu, A. J. Liang, C. Chen, S. W. Jung, C. Cacho, Y. H. Mao, S. Liu, M. X. Wang, Y. F. Guo, Y. Xu, Z. K. Liu, L. X. Yang, and Y. L. Chen, Phys. Rev. X **9**, 041040 (2019).
[35] P. Swatek, Y. Wu, L.-L. Wang, K. Lee, B. Schrunk, J. Yan, and A. Kaminski, Phys. Rev. B **101**, 161109(R) (2020).
[36] H. Li, S.-Y. Gao, S.-F. Duan, Y.-F. Xu, K.-J. Zhu, S.-J. Tian, J.-C. Gao, W.-H. Fan, Z.-C. Rao, J.-R. Huang, J.-J. Li, D.-Y. Yan, Z.-T. Liu, W.-L. Liu, Y.-B. Huang, Y.-L. Li, Y. Liu, G.-B. Zhang, P. Zhang, T. Kondo, S. Shin, H.-C. Lei, Y.-G. Shi, W.-T. Zhang, H.-M. Weng, T. Qian, and H. Ding, Phys. Rev. X **9**, 041039 (2019).
[37] D. A. Estyunin, I. I. Klimovskikh, A. M. Shikin, E. F. Schwier, M. M. Otrokov, A. Kimura, S. Kumar, S. O. Filnov, Z. S. Aliev, M. B. Babanly, and E. V. Chulkov, APL Mater. **8**, 021105 (2020).
[38] K. Y. Chen, B. S. Wang, J.-Q. Yan, D. S. Parker, J.-S. Zhou, Y. Uwatoko, and J.-G. Cheng, Phys. Rev. Mater. **3**, 094201 (2019).
[39] H. Li, S. Liu, C. Liu, J. Zhang, Y. Xu, R. Yu, Y. Wu, Y. Zhang, and S. Fan, Phys. Chem. Chem. Phys. **22**, 556 (2020).
[40] See Supplemental Material at http://link.aps.org/supplemental/10.1103/PhysRevB.103.L121103 for the details about the experimental methods, Drude-Lorentz analysis, additional data, band calculations, and multiband approach, which includes Refs. [41–44].
[41] C. C. Homes, M. Reedyk, D. A. Cradles, and T. Timusk, Appl. Opt. **32**, 2976 (1993).
[42] M. Dressel and G. Grüner, *Electrodynamics of Solids* (Cambridge University Press, Cambridge, 2002).
[43] J. Korringa, Physica **16**, 601 (1950).
[44] S. Barnes, Adv. Phys. **30**, 801 (1981).
[45] Z. A. Jahangirli, E. H. Alizade, Z. S. Aliev, M. M. Otrokov, N. A. Ismayilova, S. N. Mammadov, I. R. Amiraslanov, N. T. Mamedov, G. S. Orudjev, M. B. Babanly, A. M. Shikin, and E. V. Chulkov, J. Vac. Sci. Technol. B **37**, 062910 (2019).
[46] S. V. Dordevic, M. S. Wolf, N. Stojilovic, H. Lei, and C. Petrovic, J. Phys.: Condens. Matter **25**, 075501 (2013).
[47] P. Tang, Q. Zhou, G. Xu, and S.-C. Zhang, Nat. Phys. **12**, 1100 (2016).
[48] J. R. Drabble, Proc. Phys. Soc. **72**, 380 (1958).
[49] H. J. Goldsmid, Proc. Phys. Soc. **71**, 633 (1958).
[50] N. Chand, T. Henderson, J. Klem, W. T. Masselink, R. Fischer, Y.-C. Chang, and H. Morkoc, Phys. Rev. B **30**, 4481 (1984).
[51] D. Carter and R. Bate, *The Physics of Semimetals and Narrow-gap Semiconductors: Proceedings*, supplement to J. Phys. Chem. Solids (Pergamon, Oxford, 1971).
[52] *Electrons and Phonons in Layered Crystal Structures*, edited by T. J. Wieting and M. Schlüter (Springer, Dordrecht, 1979).
[53] G. A. Thomas, D. H. Rapkine, R. B. Van Dover, L. F. Mattheiss, W. A. Sunder, L. F. Schneemeyer, and J. V. Waszczak, Phys. Rev. B **46**, 1553 (1992).